

Macro-Scale Electrostatic Origami Motor

Alex S. Miller

*Dept. of Aeronautics and Astronautics
Massachusetts Institute of Technology
Cambridge, USA
asmiller@mit.edu*

Leo McElroy

*Independent Researcher
Cambridge, USA
leomcelroy@gmail.com*

Jeffrey H. Lang

*Dept. of Electrical Eng. and Computer Sci.
Massachusetts Institute of Technology
Cambridge, USA
lang@mit.edu*

Abstract—Foldable robots have been an active area of robotics research due to their high volume-to-mass ratio, easy packability, and shape adaptability. For locomotion, previously developed foldable robots have either embedded linear actuators in, or attached non-folding rotary motors to, their structure. Further, those actuators directly embedded in the structure of the folding medium all contributed to linear or folding motion, not to continuous rotary motion. On the macro-scale there has not yet been a folding continuous rotary actuator. This paper details the development and testing of the first macro-scale origami rotary motor that can be folded flat, and then unfurled to operate. Using corona discharge for torque production, the prototype motor achieved an expansion ratio of 2.5:1, reached a top speed of 1440 rpm when driven at -29 kV, and exhibited a maximum output torque over 0.15 mN m with an active component torque density of 0.04 N m kg⁻¹.

Index Terms—origami, motor, folding, robot, space

I. INTRODUCTION

Origami has enabled robots to change form [1] [2], to pack into smaller sizes, and to achieve a high volume-to-mass ratio [3]. Locomotion in origami robotics applications remains difficult due to the necessity of thin materials. Existing origami robots have been actuated by external fields [2] [4], by non-folding attached rotary motors [5] [6], by cable actuation [7], or by linear actuators on the origami structure such as shape memory alloy [8] and super-coiled conductive polymer actuators [9]. Folding structures have contributed to useful advances in space structures, rovers, and satellites; since space systems are launched in a fixed volume, origami enables small stowed packages to transform into large structures [3] [10] [11].

Electrostatic motors and other electric-field machines have captured the attention of actuator designers since the 1740s [12]. Electric-field machines may be built using variable capacitance, electrostatic induction, permanent electrets, or corona discharge as the active mechanism of torque production [12]. Electric fields rather than magnetic fields are the clear choice for implementing a foldable rotary actuator, since electrodes are far easier to fabricate in a 2D form than magnets or coils. Electric-field machines favor high surface area of material, whereas magnetic field machines favor high volume of material. An electrostatic motor made using DNA origami

techniques was recently demonstrated on the nano scale, but this motor was not readily collapsible after construction [13]. In this paper, we design and demonstrate a corona motor that is the first macro-scale origami motor, and the first collapsible continuous rotary motor. A photograph of the assembled origami motor in this work is shown in Fig. 1.

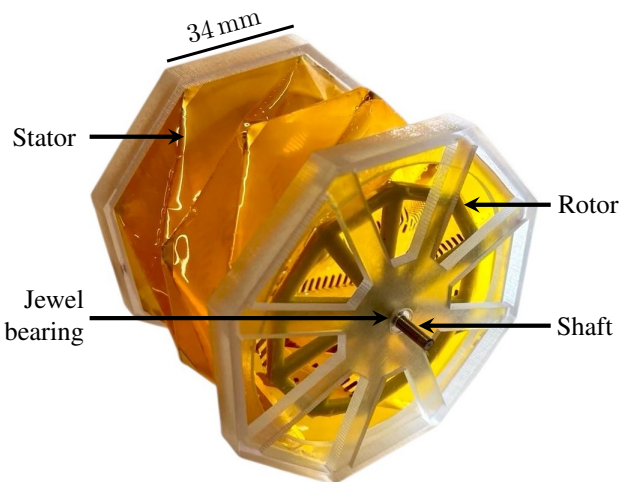


Fig. 1. Assembled electrostatic origami motor.

II. DESIGN

To achieve a folding origami motor with radial electric fields requires two nested collapsible cylindrical patterns. There are many possibilities for achieving collapsible cylindrical origami, including a Kresling [14], Yoshimura [15] [16], Tachi-Miura [17], or Waterbomb cylinder tesselation [18]. For this application, a Kresling pattern is selected due to its well-known geometric design constraints and the varying stability possibilities that the pattern offers [18] [19]. Particularly, the Kresling pattern has high resistance to axial bending which aids bearing design, enabling a more precise electrostatic gap than other origami patterns. The Kresling pattern in this work was designed to be monostable in the deployed position, but future designs could use bistable Kresling patterns to enable more sophisticated deployment schemes.

One of the cylinders, the rotor, is rigidly fixed onto central shafts at both ends. The other cylinder, the stator, nests outside of the rotor with bearings on the shaft at both ends to

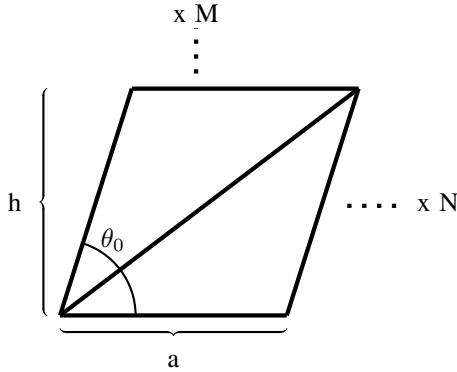


Fig. 2. Key dimensions in the mechanism unit cell design.

support radial and axial forces. To enable precise fabrication of electrodes onto their flexible surfaces, the rotor and stator are fabricated with flexible printed-circuit boards (flexPCBs); paper and conductive tape are effective in the prototyping process. To enable operation with a direct-current power supply, the motor presented in this paper is designed as a corona discharge motor. Thus, the stator has electrodes that are excited by a high-voltage power supply, and the rotor is completely passive.

The geometry of the rotor and stator are defined by the radius of the inscribed circle of the Kresling cylinder, R , the number of segments around the circumference, N , and θ_0 , the angle between the base and diagonal of the parallelogram unit cell. A diagram of a single unit cell is shown in Fig. 2. The side length of each unit is calculated as

$$a = 2R \sin\left(\frac{\pi}{N}\right). \quad (1)$$

Then, as Lang and Zang [18] [19] note, the angle between the consecutive polygons in the folded configuration is

$$\theta_{\max} = \pi - \frac{2\pi}{N} - \theta_0. \quad (2)$$

By Lang and Zang [18] [19], this sets the height of the unit cell at

$$h = R\sqrt{2[\cos(\theta_0) - \cos(\theta_{\max})]}. \quad (3)$$

The stator and rotor support electrode patterns which enable the device to function as a motor. The stator employs strip electrodes on the inside of the flexPCB, positioned on the long diagonals which stick in towards the rotor. These electrodes are positioned on the inner-most surfaces of the stator to minimize the gap from the stator to the rotor, and to act as a sharp surface which concentrates the electric field, thus promoting corona discharge.

The rotor has a series of pads on top of an insulating substrate which collect corona discharge from the stator. These pads are placed on the short vertical sides which stick out most prominently from the rotor exterior. These pads are segmented to prevent shorting from different areas of the motor, since both the rotor and stator are slanted. The rotor and stator electrode patterns are replicated N times circumferentially and

TABLE I
KEY DIMENSIONS IN STATOR AND ROTOR.

	Stator Dimension	Rotor Dimension
R	41 mm	30 mm
θ_0	57°	57°
N	8	10
M	2	2

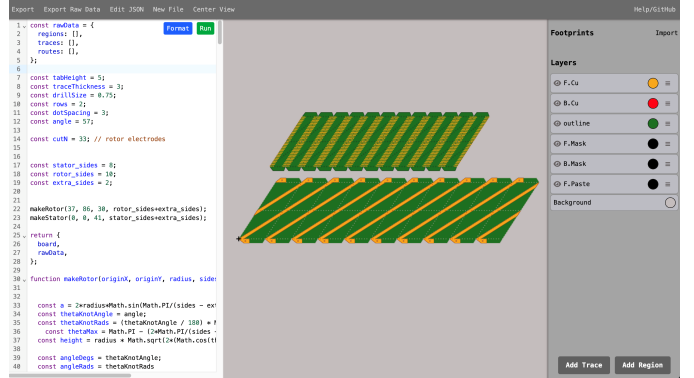


Fig. 3. The flexible circuit boards for the rotor and stator are designed in JSON-PCB, an open source script-based PCB design tool especially suited to parametric designs [20] [21].

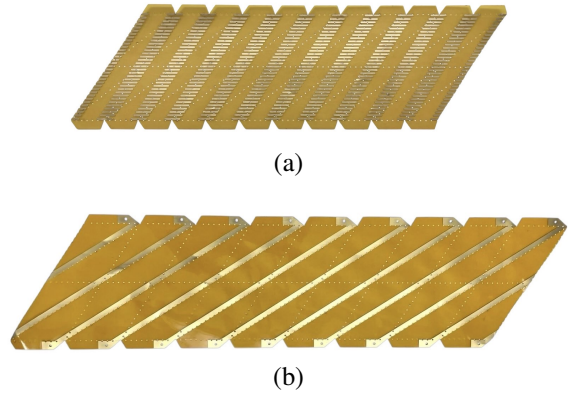


Fig. 4. The (a) rotor and (b) stator printed circuit boards.

M times axially. Tabs are added to the top and bottom of each pattern which attach to rigid components and terminal electrodes, and perforations are used to encourage clean folds. The rotor and stator sizes are chosen so that the rotor can spin freely within the stator in the fully deployed configuration.

The design is implemented in JSON-PCB, an open-source scripting tool for designing printed circuit boards [20] [21], seen in Fig. 3. The main structures have dimensions shown in Table I. To allow the PCBs to join in a cylindrical shape, with a glued overlap region, the circuit boards are manufactured with a horizontal extent of $N+1$. The rotor is manufactured on bare polyimide with no overlay, and the stator is manufactured with overlay everywhere except the electrode region. The manufactured flexPCBs are depicted in Fig. 4.

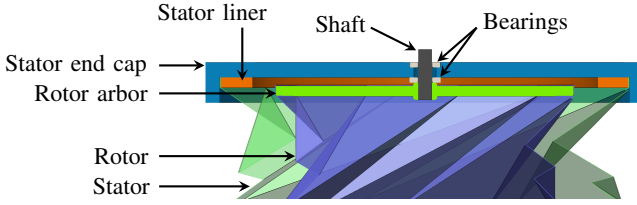


Fig. 5. Cross section of origami motor computer rendering with components labeled. The Kresling structure was generated using a CAD script [22] and adjusted to system constraints.

Rigid 3D-printed parts connect the rotor and stator to their respective bearing and shaft surfaces. These rigid components hold sapphire jewel bearings which enable low-friction motor operation. At one end of the rotor, a plastic bushing is fitted with an interference fit to the shaft to transmit the motor output power. At the other end, a ring jewel is fitted to facilitate collapsibility. Both sides of the stator are fitted with ring jewel bearings that have olive-shaped holes to allow for acceptable performance with high misalignment. A cross-section rendering showing the interfaces between the rigid and origami parts is depicted in Fig. 5.

III. ANALYSIS

A corona motor is an electrostatic machine where electric discharge from sharp features on the stator causes charge transport in ionized gas towards the rotor; this charge transport causes electrostatic repulsion, resulting shear force and rotary motion. For making simple models, corona motors may be considered a subset of electrostatic induction machines, where the gap conductivity is higher than the rotor conductivity and the excitation is constant. Rotating induction machines in a constant electric field were first characterized by von Quincke [23]; later, Melcher presented a general solution and discussion of the dynamics of electrostatic induction machines [24]. To use the induction-motor analogy for a corona motor, previous studies have estimated an effective conductivity in the gap to model the ionized air [25]. Compared to traditional electrostatic induction motors, corona motors such as the one constructed here usually have discharge blades set at an angle, where the corona discharge originates from the edge of the blade, but the field is centered around the middle of the blade structure. The method presented here accounts for this asymmetry. A graphical depiction of the model with the physical parameters and the electromechanical parameters is shown in Fig. 6. This model is appropriate when only two opposing terminals are excited; if more terminals are used, then a different form of the potential would be needed.

In cylindrical coordinates, where r is the distance from the center, z is the displacement along the motor shaft, and ϕ is the azimuthal angle, the electric potential outside the rotor can be modeled as

$$\Phi_a = \text{Re} \left(-E_0 r e^{j\phi} + \frac{\hat{A}}{r} e^{j\phi} \right), \quad (4)$$

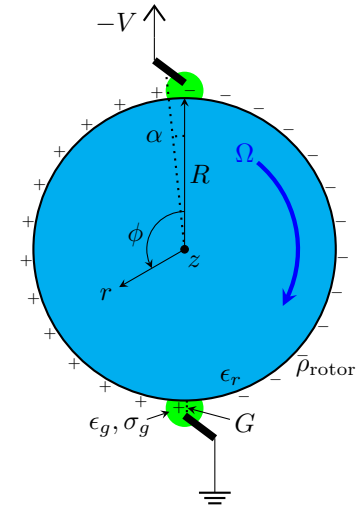


Fig. 6. A graphical representation of the corona discharge mechanism which causes motor torque with physical parameters labeled. The rotor is pictured in blue, the two stator electrodes are depicted with thick dark lines outside of the rotor surface, and ionized air is shown in green.

where E_0 is the background electric field and \hat{A} is a complex coefficient representing dipole charging of the rotor to be derived from the boundary conditions. Inside the rotor, the potential can be modeled as

$$\Phi_b = \text{Re} \left(-\hat{B} r e^{j\phi} \right), \quad (5)$$

where \hat{B} is a complex coefficient to be derived from the boundary conditions. On the surface of the rotor, where $r = R$, continuity of the electric potential dictates $\Phi_a|_{r=R} = \Phi_b|_{r=R}$, yielding a relationship between \hat{A} and \hat{B} where

$$E_0 = \frac{\hat{A}}{R^2} + \hat{B}. \quad (6)$$

Using the electric fields $E_a = -\nabla\Phi_a$ and $E_b = -\nabla\Phi_b$, charge conservation on the rotor surface yields

$$\hat{r} \cdot (\sigma E_a)|_{r=R} + \left(\frac{\partial}{\partial t} + \Omega \frac{\partial}{\partial \phi} \right) \rho_{\text{rotor}} + J_c e^{j(\phi-\alpha)} = 0, \quad (7)$$

where Ω is the rotor angular velocity, σ is the conductivity around the gap, ρ_{rotor} is the rotor surface charge, and $J_c e^{j(\phi-\alpha)}$ is the surface current density, periodic around the rotor, caused by the corona discharge. This boundary condition uses both J_c and σE_0 as modes of charge transport, modeling the charge-relaxation behavior of the rotor using σ and the charging asymmetry using J_c . The boundary condition may also be set up such that the charge relaxation term is $\hat{\phi} \cdot (\sigma E_a)|_{r=R}$; this gives the same torque result. The charge on surface of the rotor at $r = R$ may be expressed as

$$\rho_{\text{rotor}} = \text{Re} \left\{ \left[\epsilon_g \left(E_0 + \frac{\hat{A}}{R^2} \right) - \epsilon_r \hat{B} \right] e^{j\phi} \right\}, \quad (8)$$

where ϵ_g is the permittivity in the gap and ϵ_r is the permittivity of the rotor.

In steady state where $\frac{\partial \rho_{\text{rotor}}}{\partial t} = 0$, (7) can be written as

$$\sigma \left(E_0 + \frac{\hat{A}}{R^2} \right) + j\Omega \left[\epsilon_g \left(E_0 + \frac{\hat{A}}{R^2} \right) - \epsilon_r \hat{B} \right] + J_c e^{-j\alpha} = 0, \quad (9)$$

Combining (6) and (9) yields

$$\hat{A} = R^2 \frac{-E_0 [\sigma + j\Omega(\epsilon_g - \epsilon_r)] + J_c e^{-j\alpha}}{\sigma + j\Omega(\epsilon_g + \epsilon_r)}. \quad (10)$$

Substituting (6) and (10) into (8), the charge on the surface of the rotor at $r = R$ may be calculated as

$$\rho_{\text{rotor}} = \frac{-(\epsilon_g + \epsilon_r)}{1 + \Omega^2 \tau^2} \frac{J_c}{\sigma} [\cos(\phi - \alpha) + \Omega \tau \sin(\phi - \alpha)] - \frac{2\epsilon_r}{1 + \Omega^2 \tau^2} E_0 [\cos(\phi) + \Omega \tau \sin(\phi)], \quad (11)$$

where τ is a time constant, $\tau = \frac{\epsilon_r + \epsilon_g}{\sigma_g}$. The value of the electromagnetic stress tensor may be evaluated and integrated on the surface of the rotor to calculate rotor torque as

$$\mathcal{T}_{\text{motor,offset}} = R \int_0^{2\pi} \epsilon_g E_{a,r} |_{r=R} E_{a,\phi} |_{r=R} L R d\theta \\ = 2\pi L R^2 \frac{2 \frac{\epsilon_r \epsilon_g}{\epsilon_g + \epsilon_r} E_0^2 \Omega \tau + \epsilon_g E_0 \frac{J_c}{\sigma} [\sin(\alpha) + \Omega \tau \cos(\alpha)]}{1 + \Omega^2 \tau^2}, \quad (12)$$

where R is the rotor radius and L is the rotor axial length. The angular offset α gives rise to a starting torque. The maximum torque is also a function of this asymmetry and is given by

$$\mathcal{T}_{\text{motor}}_{\text{max}} = \pi L R^2 \left[\frac{2\epsilon_r \epsilon_g E_0^2}{\epsilon_r + \epsilon_g} + \epsilon_g E_0 \frac{J_c}{\sigma} (1 + \sin(\alpha)) \right]. \quad (13)$$

In this case, the “background” electric field is dependent on the size of the stator. A constitutive equation for an “effective” electric field suitable for estimating torque can be written as

$$E_{0,\text{eff}} \approx \frac{J_c}{\sigma} \approx \frac{V - V_{\text{onset}}}{2R + 2G}, \quad (14)$$

where V is the driving voltage and V_{onset} is a correction term for the voltage at which discharge begins. The V_{onset} offset depends on atmospheric conditions and the gap. For example, under standard conditions, a breakdown voltage of $\approx 3 \text{ kV mm}^{-1}$ would be typical.

IV. ASSEMBLY

All 3D printed parts are printed on a Stratasys J5 MediJet printer with dissolvable supports. For the rotor assembly, the flexPCB rotor is adhered to rigid components at both ends using double-sided tape. This taping is performed by first wrapping the tape around the rigid rotor attachments, then rolling the rotor around them, with a temporary stabilizing shaft as shown in Fig. 7. The stabilizing shaft is then removed and the two end-shafts are pre-fit into an interference fit on the rotor assembly. There is one unit of overlap in the rotor, which is filled with double sided tape. Cyanacrylate adhesive

is added near the taping surface to further increase rigidity and the overhang is trimmed.

Before the stator is assembled, the stator flexPCB is laminated with a single sheet of polyimide (Kapton) tape on the outer side. The design of the stator features copper pours at the edge of fold lines which create mechanical stress concentrations; earlier prototypes without lamination exhibited cracking, which is alleviated by this lamination step. The lamination is made only on the outside surface of the stator, and with near full coverage, leaving a set of terminal pads exposed to connect power to the motor.

For the stator assembly, the flexPCB stator is adhered to the rigid liner component at both ends with double-sided tape using the same rolling technique as the rotor. At one end of the stator assembly, after fitting the liner, 1 cm copper strips, serving as power terminals, are fitted to two opposing rotor electrodes that do not pass over the edges of the flexPCB. A ring jewel bearing is then fitted into each stator end cap.

Next, the full motor is assembled. Ring jewel bearings are fitted into each stator end cap to handle radial loads. From bottom to top, the following components are stacked: a stator end cap, the stator with a liner ring, one thrust bearing, the rotor assembly with the plastic bushing down, one more thrust bearing, then the remaining stator end cap. All bearings are the SwissJewel R317.0 model [26] olive-shaped ring jewel. Depending on the folding precision achieved, a second set of thrust bearings may be added to further constrain the rotor if needed. Finally, the bearings are lubricated with Moebius 9020 watch lubricant, dispensed using a 31-gauge syringe. The completed assembly is shown in Fig. 1. The collapse and stowing action is shown in Fig. 8, with the system achieving a stowed height of 26.5 mm and a deployed height of 66.0 mm.

V. TESTING AND RESULTS

The motor was connected to a high-voltage DC power supply, with a pair of opposite motor electrodes connected to power and ground and with a current limit of 0.5 mA for safety. All data were collected with the central axis of the motor perpendicular to gravity. Movies of motor rotation were taken using an Edgertronic SC1 Monochrome high-speed camera, recording at 2000 fps. These frame data were processed using the Tracker Video Analysis and Modeling Tool to track a small dot on the rotor. Angular velocity and acceleration were calculated from position measurements of the dot in each frame. The motor was able to self start repeatedly at voltages exceeding -27.5 kV in amplitude. For these voltages, time-series data are shown in Fig. 9, where the motor was powered on at a fixed DC voltage, then powered off. A weak mechanical instability was observed in the -29 kV trial likely due to the rotor moving axially towards the stator end cap. When started from rest, the motor always started in the same direction. When the motor was manually started in the other direction, it operated in a reverse-direction mode with a lower-speed, further supporting the model developed in Section III.

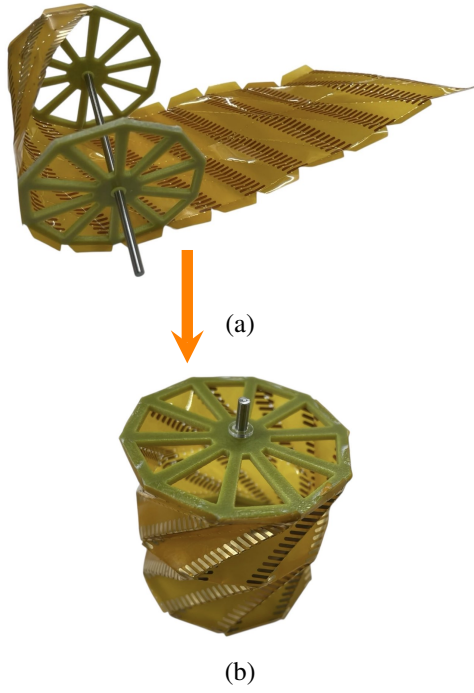


Fig. 7. Assembly of rotor structure. First, in (a) the rotor is wrapped around a rigid arbor and affixed with double sided tape, with a full-length alignment shaft. Then the connections are glued, the edges are trimmed, and partial-length shafts are installed, leading to the finished rotor in (b).

From the time-series data in Fig. 9, the output torque can be calculated as

$$\mathcal{T}_{\text{output}} = I_{\text{rotor}} \frac{d^2\theta}{dt^2}, \quad (15)$$

where I_{rotor} is the moment of inertia and θ is the rotation angle of the spinning rotor. In the prototype tested here, $I_{\text{rotor}} = 4.24 \times 10^{-6} \text{ kg m}^2$. The total output torque, $\mathcal{T}_{\text{output}}$, is the sum of the active motor torque, $\mathcal{T}_{\text{motor}}$, and the load torque of bearing friction and aerodynamic drag, $\mathcal{T}_{\text{load}}$ where

$$\mathcal{T}_{\text{output}} = \mathcal{T}_{\text{motor}} - \mathcal{T}_{\text{load}}. \quad (16)$$

After power is disconnected from the motor, $\mathcal{T}_{\text{output}} = -\mathcal{T}_{\text{load}}$. Therefore, the spin-down phase was used to characterize the bearing and windage loads in the motor. In Fig. 10, the spin-down load torque is plotted and a quadratic load curve is fitted. This technique characterizes dynamic friction, but not static friction, since the system is in motion during spin-down.

From the characterization of $\mathcal{T}_{\text{load}}$, $\mathcal{T}_{\text{motor}}$ was calculated for various driving voltage levels, shown in Fig. 11. The motor is able to run at speeds where the torque is above the load curve during speed-up, and reaches a steady state when the motor speed intersects the load curve. Oscillations in speed due to mechanical factors, such as occasional axial rotor movement, were present, especially in the -29 kV trial. These measurements were plotted alongside the model developed

in Section III, Eqs. (12) and (14) with the parameters $\sigma = 2 \text{ nS m}^{-1}$, $R = 30 \text{ mm}$, $L = 52 \text{ mm}$, $G = 3.5 \text{ mm}$, $\epsilon_g = \epsilon_0$, $\epsilon_r = \epsilon_0$, $V_{\text{onset}} = -10.5 \text{ kV}$, and $\alpha = 0.15 \text{ rad}$. This value of σ is identical to that found by Krein [25], and the value for V_{onset} is consistent with the size of the gap, G . This model shares key characteristics with these data, having comparable zero-speed torque and maximum torque.

In addition to the measurements made during the full speed-up and slow-down, measurements were also recorded once the motor reached steady state. These data were taken by first starting the motor at -29 kV , waiting for the motor to reach steady state, taking a video measurement, then decreasing the magnitude of excitation by 0.5 kV , waiting for the motor to reach steady state, and taking a new measurement. This process was repeated until the motor was no longer able to run continuously, which occurred below -19 kV amplitude. This experimental process allowed access to lower voltage operating points than would be accessible starting from rest due to the static friction of the bearing being greater than the dynamic friction. These measurements are shown in Fig. 12.

Using the load curve from the spin-down tests, these data were transformed to represent the steady state motor torque, $\mathcal{T}_{\text{motor}}$ at the same voltages as shown in Fig. 13. These measurements are compared to the model developed in Section III, Eqs. (13) and (14), and are similar in shape and magnitude.

The assembled origami motor was able to deploy from a stowed body height of 26.5 mm to a deployed body height of 66.0 mm , resulting in a body expansion ratio of $2.5:1$. Mechanically, the rotor was folded more than 50 times without visible damage. The stator, and correspondingly, the whole motor, was folded more than 5 times before cracking began to appear on the stator electrodes. The motor reached a maximum speed of 1440 rpm when driven at -29 kV as shown in Fig. 12 and produced over 0.2 mN m of motor torque, $\mathcal{T}_{\text{motor}}$, as shown in Fig. 13. The maximum output torque, $\mathcal{T}_{\text{output}}$, was measured at 0.15 mN m , as seen in the difference between the motor torque and load curves in Fig. 11. With a deployed volume of 0.00037 m^3 , and stowed volume of 0.00015 m^3 , the prototype motor exhibited a volumetric torque density of 0.54 N m m^{-3} in the deployed configuration, which increased to 1.35 N m m^{-3} in the stowed configuration. Considering a total system mass of 45.0 g , the motor demonstrated a torque density of $0.004 \text{ N m kg}^{-1}$, and considering only the active circuit board components with a mass of 1.38 g for the rotor and 3.30 g for the unlaminated stator, the motor demonstrated a torque density of 0.04 N m kg^{-1} .

VI. DISCUSSION

This paper presents the first macro-scale origami rotary motor. Devices like this may be useful for soft robotics applications where the robot must fit into a small packed size and then operate in a deployed state. In addition, this motor has been collapsed and deployed repeatedly without damage. Additionally, this work shows that electrostatic rotary motors can be implemented using flexible materials.

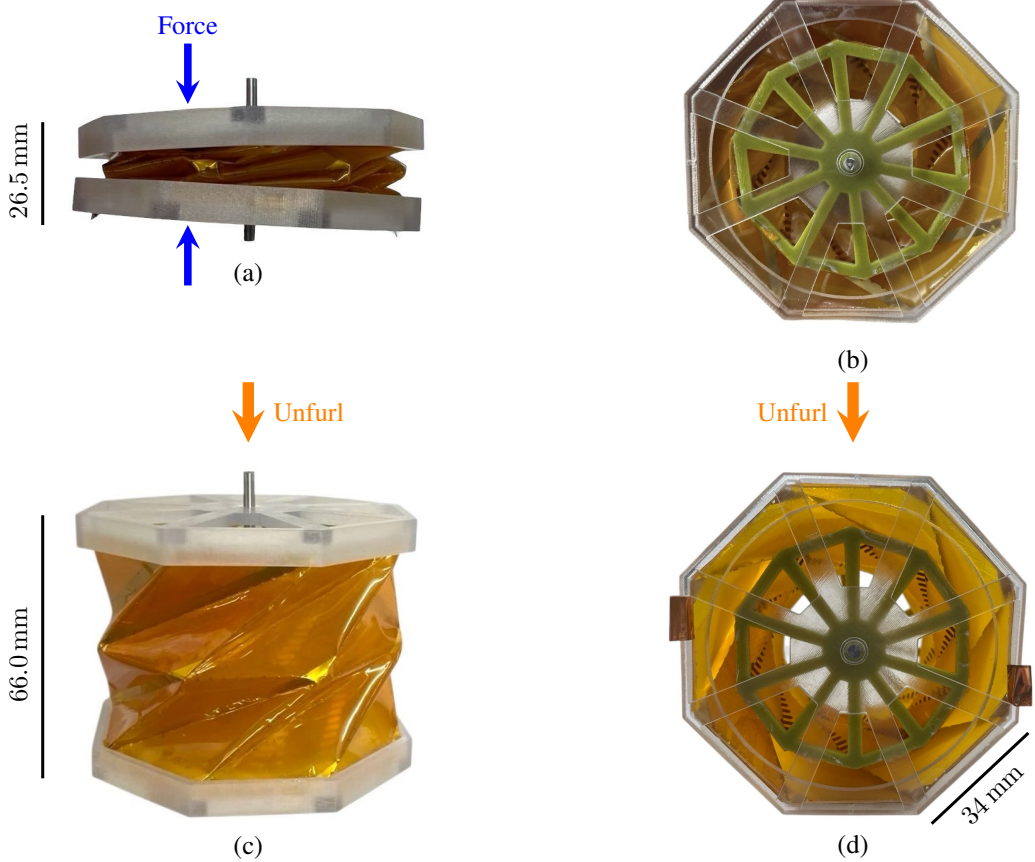


Fig. 8. The body of the electrostatic origami motor unfurls from 26.5 mm to 66.0 mm, not including external shaft height, which stays constant through the expansion and may be an arbitrary length. The stowed configuration is shown in side view and top view in (a) and (b) respectively, and the stable unfurled configuration is shown in side view and bottom view in (c) and (d) respectively. The stowed configuration is maintained by external force; after unfurling, the motor is stable in the deployed position.

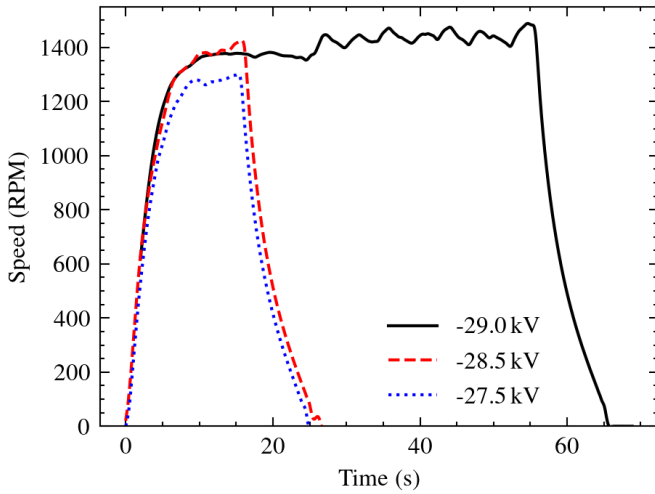


Fig. 9. Speed data time-series collected with high-speed camera. The motor was powered on and then powered off and allowed to spin down to rest. The -29 kV trial was run for longer arbitrarily, and shows oscillations in speed due to the rotor periodically moving axially towards the stator end cap.

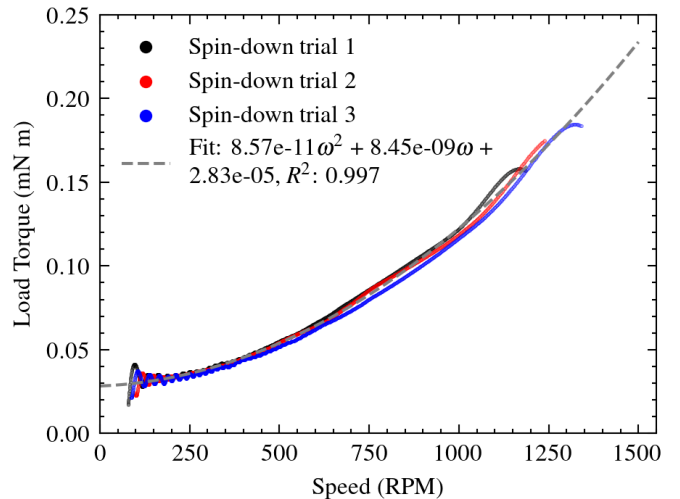


Fig. 10. Torque from bearing friction and air resistance during three unpowered spin-down tests with a corresponding fitted load curve. These data show the bearing and windage loads to be time invariant across multiple trials.

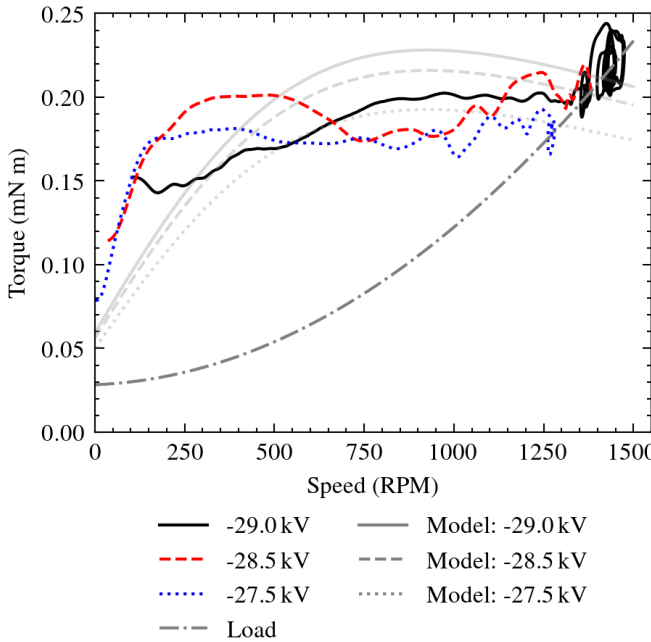


Fig. 11. Torque-speed curve of active motor components tested at three different voltages with the load subtracted. The motor increases in speed until it intersects the load curve; at this point it will stay in steady state. Minor oscillations around the steady state appear near the load curve intersection. The data are compared to the model developed in Section III, Eqs. (12) and (14), with parameters $\sigma = 2 \text{ nS m}^{-1}$, $R = 30 \text{ mm}$, $L = 52 \text{ mm}$, $G = 3.5 \text{ mm}$, $\epsilon_g = \epsilon_0$, $\epsilon_r = \epsilon_0$, $V_{\text{onset}} = -10.5 \text{ kV}$, and $\alpha = 0.15 \text{ rad}$.

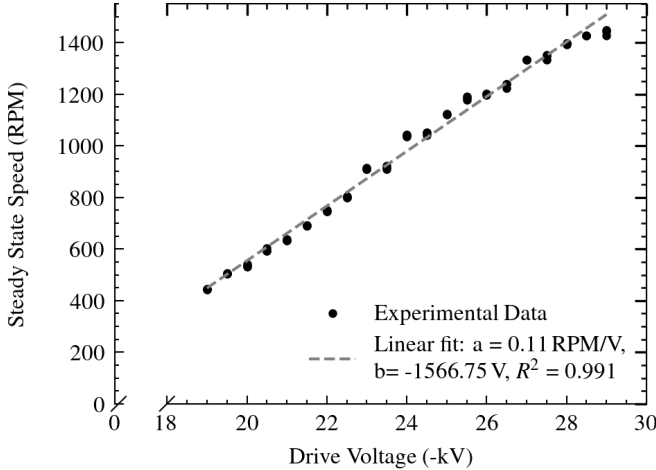


Fig. 12. Observed steady state speed as a function of drive voltage plotted with a linear fit.

While this work is useful in demonstrating the merits of electrostatic folding machines, there are several notable areas for future work. Future folding motors may be made with lower-profile rigid components and different folding patterns that enable a lower-volume folded state towards the goal of increasing volumetric torque density. New designs may also be made with tighter gaps between the rotor and stator by having more folded unit cells, and thus making them closer to cylindrical.

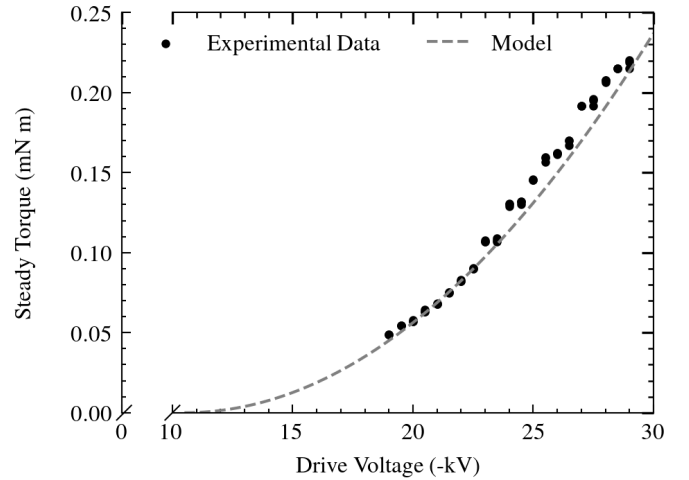


Fig. 13. Steady state torque by motor active components as a function of voltage compared to model developed in Section III, Eqs. (13) and (14) with parameters $R = 30 \text{ mm}$, $L = 52 \text{ mm}$, $G = 3.5 \text{ mm}$, $\epsilon_g = \epsilon_0$, $V_{\text{onset}} = -10.5 \text{ kV}$, and $\alpha = 0.15 \text{ rad}$.

cylindrical. Additionally, taller machines can be made by stacking more than two unit cells, yielding linearly more torque. Future designs may also incorporate latching mechanisms to allow the motor to be deployed as part of a robotic system. The motor presented was constructed using corona discharge to produce torque with a direct-current supply. Alternatively, folding motors may also be built around a variable-capacitance or electrostatic induction topology, driven with multiple phases of high-voltage alternating current, opening up possibilities for higher torque and useful control schemes.

VII. ACKNOWLEDGMENTS

A.M. and L.M. acknowledge Erik Demaine and the MIT Origami Folding Algorithms class for learning, inspiration, and guidance. The team thanks Jim Bales for lending high-speed videography and lighting equipment. The authors thank the T.J. Rodgers RLE Laboratory for their helpful equipment and advice.

REFERENCES

- [1] E. Hawkes, B. An, N. M. Benbernou, H. Tanaka, S. Kim, E. D. Demaine, D. Rus, and R. J. Wood, "Programmable matter by folding," *Proceedings of the National Academy of Sciences*, vol. 107, no. 28, pp. 12441–12445, Jul. 2010.
- [2] S. Miyashita, S. Guitron, M. Ludersdorfer, C. R. Sung, and D. Rus, "An untethered miniature origami robot that self-folds, walks, swims, and degrades," in *2015 IEEE international conference on robotics and automation (ICRA)*. IEEE, 2015, pp. 1490–1496.
- [3] M. Meloni, J. Cai, Q. Zhang, D. Sang-Hoon Lee, M. Li, R. Ma, T. E. Parashkevov, and J. Feng, "Engineering Origami: A Comprehensive Review of Recent Applications, Design Methods, and Tools," *Advanced Science*, vol. 8, no. 13, p. 2000636, 2021.
- [4] Q. Ze, S. Wu, J. Dai, S. Lanza, G. Ikeda, P. C. Yang, G. Iaccarino, and R. R. Zhao, "Spinning-enabled wireless amphibious origami millirobot," *Nature Communications*, vol. 13, no. 1, p. 3118, Jun. 2022, publisher: Nature Publishing Group. [Online]. Available: <https://www.nature.com/articles/s41467-022-30802-w>
- [5] C. Sung and D. Rus, "Foldable Joints for Foldable Robots," *Journal of Mechanisms and Robotics*, vol. 7, no. 2, p. 021012, May 2015.

- [6] J. Carlson, J. Friedman, C. Kim, and C. Sung, “REBOund: Untethered Origami Jumping Robot with Controllable Jump Height,” in *2020 IEEE International Conference on Robotics and Automation (ICRA)*. Paris, France: IEEE, May 2020, pp. 10 089–10 095.
- [7] M. Ochalek, A. Haraszti, and M. Arya, “Adaptive Stiffness and Shape Control of a Modular Origami-Inspired Robot,” Jul. 2024.
- [8] K. Hu, K. Rabenorosoa, and M. Ouisse, “A Review of SMA-Based Actuators for Bidirectional Rotational Motion: Application to Origami Robots,” *Frontiers in Robotics and AI*, vol. 8, p. 678486, Jul. 2021.
- [9] W. Yan, S. Li, M. Deguchi, Z. Zheng, D. Rus, and A. Mehta, “Origami-based integration of robots that sense, decide, and respond,” *Nature Communications*, vol. 14, no. 1, p. 1553, Apr. 2023.
- [10] N. Turner, B. Goodwine, and M. Sen, “A review of origami applications in mechanical engineering,” *Proceedings of the Institution of Mechanical Engineers, Part C: Journal of Mechanical Engineering Science*, vol. 230, no. 14, pp. 2345–2362, Aug. 2016, publisher: IMECEH.
- [11] H. Gong and S. Gong, “Design of foldable PCBSat enabling three-axis attitude control,” *Acta Astronautica*, vol. 192, pp. 291–300, Mar. 2022.
- [12] O. Jefimenko, *Electrostatic Motors: Their History, Types and Principles of Operation*, 1st ed., T. Valone, Ed. Integrity Research Institute, Mar. 2011.
- [13] A.-K. Pumm, W. Engelen, E. Kopperger, J. Isensee, M. Vogt, V. Kozina, M. Kube, M. N. Honemann, E. Bertosin, M. Langecker, R. Golestanian, F. C. Simmel, and H. Dietz, “A DNA origami rotary ratchet motor,” *Nature*, vol. 607, no. 7919, pp. 492–498, Jul. 2022.
- [14] B. Kresling, “Natural twist buckling in shells: from the hawkmoth’s bellow to the deployable Kresling-pattern and cylindrical Miura-ori,” *IASS-IACM 2008 Spanning Nano to Mega*, Jan. 2008.
- [15] Y. Yoshimura, “On the mechanism of buckling of a circular cylindrical shell under axial compression,” Jul. 1955, nTRS Author Affiliations: University of Tokyo NTRS Report/Patent Number: NACA-TM-1390 NTRS Document ID: 19930093840 NTRS Research Center: Legacy CDMS (CDMS).
- [16] T. Von Karman and H.-S. Tsien, “The Buckling of Thin Cylindrical Shells Under Axial Compression,” *Journal of the Aeronautical Sciences*, vol. 8, no. 8, pp. 303–312, Jun. 1941, publisher: American Institute of Aeronautics and Astronautics.
- [17] T. Tachi, “One-DOF cylindrical deployable structures with rigid quadrilateral panels,” *Proc. IASS Symp.*, Jan. 2010.
- [18] R. J. Lang, *Twists, Tilings, and Tessellations: Mathematical Methods for Geometric Origami*. New York: A K Peters/CRC Press, Dec. 2017.
- [19] S. Zang, D. Misseroni, T. Zhao, and G. H. Paulino, “Kresling origami mechanics explained: Experiments and theory,” *Journal of the Mechanics and Physics of Solids*, vol. 188, p. 105630, Jul. 2024.
- [20] leomcelroy, “leomcelroy/JSON-PCB,” Apr. 2025, original-date: 2024-09-30T04:51:15Z. [Online]. Available: <https://github.com/leomcelroy/JSON-PCB>
- [21] L. McElroy, Q. Bolsée, N. Peek, and N. Gershenfeld, “Svg-pcb: a web-based bidirectional electronics board editor,” in *Proceedings of the 7th Annual ACM Symposium on Computational Fabrication*, 2022, pp. 1–9.
- [22] N. Hanson, I. A. Mensah, S. F. Roberts, J. Healey, C. Wu, and K. L. Dorsey, “Controlling the fold: proprioceptive feedback in a soft origami robot,” *Frontiers in Robotics and AI*, vol. 11, May 2024.
- [23] G. Quincke, “Ueber Rotationen im constanten elektrischen Felde,” *Annalen der Physik*, vol. 295, no. 11, pp. 417–486, 1896, 02.
- [24] J. R. Melcher, *Continuum electromechanics*. Cambridge, Mass: MIT Press, 1981.
- [25] P. Krein, “Analysis of corona motors and micromotors by means of effective gap conductivity,” *IEEE Transactions on Industry Applications*, vol. 31, no. 4, pp. 752–760, Jul. 1995.
- [26] “Ring Jewel Bearings - R317.0.” [Online]. Available: <https://www.swissjewel.com/product/jewel-bearings/ring-jewels/r317-0/>